



**HAL**  
open science

# Effect of total pressure on La<sub>2</sub>NiO<sub>4</sub> coatings deposited by reactive magnetron sputtering using plasma emission monitoring

Jérémie Fondard, Alain Billard, Ghislaine Bertrand, Sébastien Fourcade,  
Pierre Batocchi, Fabrice Mauvy, Pascal Briois

## ► To cite this version:

Jérémie Fondard, Alain Billard, Ghislaine Bertrand, Sébastien Fourcade, Pierre Batocchi, et al.. Effect of total pressure on La<sub>2</sub>NiO<sub>4</sub> coatings deposited by reactive magnetron sputtering using plasma emission monitoring. *Surface and Coatings Technology*, 2016, 295, pp.29-36. 10.1016/j.surfcoat.2015.11.053 . hal-02430400

**HAL Id: hal-02430400**

**<https://hal.science/hal-02430400>**

Submitted on 7 Jan 2020

**HAL** is a multi-disciplinary open access archive for the deposit and dissemination of scientific research documents, whether they are published or not. The documents may come from teaching and research institutions in France or abroad, or from public or private research centers.

L'archive ouverte pluridisciplinaire **HAL**, est destinée au dépôt et à la diffusion de documents scientifiques de niveau recherche, publiés ou non, émanant des établissements d'enseignement et de recherche français ou étrangers, des laboratoires publics ou privés.



## Open Archive Toulouse Archive Ouverte (OATAO)

OATAO is an open access repository that collects the work of Toulouse researchers and makes it freely available over the web where possible

This is an author's version published in: <http://oatao.univ-toulouse.fr/24461>

**Official URL:** <https://doi.org/10.1016/j.surfcoat.2015.11.053>

### **To cite this version:**

Fondard, Jérémie and Billard, Alain and Bertrand, Ghislaine  and Fourcade, Sébastien and Batocchi, Pierre and Mauvy, Fabrice and Briois, Pascal *Effect of total pressure on La<sub>2</sub>NiO<sub>4</sub> coatings deposited by reactive magnetron sputtering using plasma emission monitoring.* (2016) *Surface and Coatings Technology*, 295. 29-36. ISSN 0257-8972

Any correspondence concerning this service should be sent to the repository administrator: [tech-oatao@listes-diff.inp-toulouse.fr](mailto:tech-oatao@listes-diff.inp-toulouse.fr)

# Effect of total pressure on $\text{La}_2\text{NiO}_4$ coatings deposited by reactive magnetron sputtering using plasma emission monitoring

J. Fondard<sup>a,b</sup>, A. Billard<sup>a,b</sup>, G. Bertrand<sup>c</sup>, S. Fourcade<sup>d</sup>, P. Batocchi<sup>d</sup>, F. Mauvy<sup>d</sup>, P. Briois<sup>a,b,\*</sup>

<sup>a</sup> IRTES-LERMPS, EA 7274, 90010 Belfort, France

<sup>b</sup> FR FCLab, 3539, 90000 Belfort, France

<sup>c</sup> CIRIMAT UMR5085, INPT-ENSIACET, 4 allée E. Monso, BP 44362, 31030 Toulouse Cedex, France

<sup>d</sup> ICMCB-CNRS, 87 Av. du Dr. A. Schweitzer, 33608 Pessac Cedex, France

## ARTICLE INFO

### Keywords:

$\text{La}_2\text{NiO}_4$

Reactive magnetron sputtering

Effect of total pressure

Intermediate-temperature solid oxide fuel cell

Complete cell tests

## ABSTRACT

This work focuses on the structural, microstructural, electrical and electrochemical characterization of  $\text{La}_2\text{NiO}_4$  coatings deposited by reactive magnetron sputtering under different argon partial pressures. Deposition was driven by Plasma Emission Monitoring system (PEM) which allows high deposition rate. For each pressure, the optimal regulation setpoint for lanthanum oxide deposition is determined and then the current dissipated on the nickel target is adjusted to obtain the convenient La/Ni ratio to achieve the  $\text{K}_2\text{NiF}_4$  structure. After an appropriate annealing treatment, coatings crystallize in the desired structure with more or less impurities. Increasing the device's pressure from 0.4 to 4.8 Pa produces more porous samples with different microstructures. Then, a coating with porosity gradient was built by using these four different total pressures. Its electrical performances were tested and allowed its utilization as cathode layer in intermediate temperature solid oxide fuel cell (IT SOFC). This modified architecture cathode allows better performances ( $71 \text{ mW} \cdot \text{cm}^{-2}$ ) than dense cathode produced by the same technique ( $51 \text{ mW} \cdot \text{cm}^{-2}$ ).

## 1. Introduction

Since solid oxide fuel cells (SOFC) are designed to operate at intermediate temperature (873–1073 K), research works try to face with the drop of the cell performances. Solutions have to be found on each active layer to reduce losses. Reducing layer's thicknesses and using new materials remain the most effective ways to solve this problem. At the cathode side, where high overpotentials cause high resistances, mixed ionic and electronic conductors (MIECs) are dedicated to be new materials. It is believed that the improvements are induced by the extended area reaction from triple phase boundary to the whole surface, reducing electrode polarization. Most studies concerning MIECs are talking about perovskite type oxides [1–5]. These compounds become the reference for cathode materials at these lower temperatures. More recently,  $\text{Ln}_2\text{NiO}_{4+\delta}$  compounds (Ln = La, Pr, Nd) with  $\text{K}_2\text{NiF}_4$  structure have been investigated as cathode material [6–10]. These structures present very good catalytic properties towards the oxygen, a predominant electronic conductivity in the whole  $p(\text{O}_2)$  range and they are chemically compatible with the electrolyte and the interconnector materials. Because of these properties, those materials have been studied in half cells with different electrolytes with promising results [11] and they begin to be used as cathode material in single cells [12].

Whereas thick layers deposited by wet techniques are commonly used as cathodes in IT SOFCs, recent studies deal with the deposition of MIEC coatings by physical surface deposition processes [13–15]. Reactive magnetron sputtering (RMS) technique allows the deposition of thin and dense layers able to be used as electrolyte [16] or diffusion barrier layers [17] in fuel cells. Recently, half cells were completely produced by this process with promising results [18]. Previous studies performed in our laboratory proved that this technique may also deposit a cathode layer by co-sputtering of several metallic targets [19–20]. Thin and dense  $\text{La}_2\text{NiO}_{4+\delta}$  layers were hence synthesized and electrically tested, revealing interesting results compared to literature [20]. Nevertheless, electrochemical characterizations and complete cell tests of this material disclose low results (i.e.  $50 \text{ mW}/\text{cm}^2$  at 973 K on Ni-YSZ/YSZ/GDC/ $\text{La}_2\text{NiO}_{4+\delta}$ ). The gas tightness of the dense cathode layer avoids a fast adsorption and diffusion of oxygen, resulting as low electrochemical characteristics as demonstrated in literature with other MIECs [21–22]. Therefore, the porosity of this layer has to be increased to improve its performances.

In this study, we investigate the feasibility of producing a thin  $\text{La}_2\text{NiO}_{4+\delta}$  coatings with a porosity gradient by RMS under unstable conditions using Plasma Emission Monitoring (PEM) [23–24]. This technique allows the deposition of oxide coatings with high sputtering rate. Four point probe electrical analyses were performed on annealed lanthanum nickelate films in static air in the temperature range from 293 to 1273 K with temperature steps and stabilization time of about

\* Corresponding author at: IRTES-LERMPS, EA 7274, 90010 Belfort, France.  
E-mail address: pascal.briois@utbm.fr (P. Briois).

25 K and 20 min, respectively. A Ni YSZ/YSZ/GDC/La<sub>2</sub>NiO<sub>4+δ</sub> complete cell was then synthesized from a commercial NiO YSZ anode support using RMS technique. Manufacture of this cell has been described in a previous study [25]. The overall cell performance and detailed impedance analyses of this cell are presented and compared to this cell presenting a dense La<sub>2</sub>NiO<sub>4+δ</sub> layer to elucidate the gain of this special configuration.

## 2. Experimental details

### 2.1. Deposition device

An Alcatel SCM 650 setup was used in this study. Fig. 1 shows a scheme of the complete setup. The desired vacuum of this 100 L volume sputtering chamber is obtained via a system using ALCATEL RSV 301B/2063 primary pump and a 5401CP turbo molecular pump. The chamber is composed by three magnetron targets (diameter = 200 mm), a rotating substrate holder ( $\varnothing = 620$  mm) and an optical fiber placed near the erosion area of the target. The distance of 110 mm between the substrate holder, parallel to the targets, was used for these experiments. A pulsed DC dual generator (Advanced Energy Pinnacle +) managed the discharge current of the targets. For each deposition with the lanthanum metallic targets, the discharge current was fixed at 2.5 A while it was varied with the nickel target to obtain a La/Ni metallic ratio of 2, and consequently the wished K<sub>2</sub>NiF<sub>4</sub> structure. Different glass, alumina ( $\varnothing = 16$  mm), YSZ ( $\varnothing = 20$  mm) samples and Ni YSZ/YSZ/GDC sputtered half cells with commercial anode support ( $\varnothing = 23$  mm), were used as substrates for the various analyses made during this work. Before to realize the cathode deposition ( $\varnothing = 21$  mm), a circular mask was placed on the half cell to allow the single measurements. Prior to each deposition, substrates were cleaned by cold soaped water, rinsed and then dried with paper. The anode supports were additionally dried at 353 K for 3 h to remove the water. Electrolyte and GDC protective films were coated in the same setup with Zr Y (84 16 at.%) and Ce Gd (80 20 at.%) metallic targets followed by a thermal treatment at 773 K for 2 h after each deposition process to densify the coatings. Substrates were placed at 170 mm of substrate holder's center, where the coatings present the best homogeneity. Argon and oxygen gases were used to obtain a plasma and deposit ceramic coatings. Flow meters (Brooks) managed the gas flow rates and Baratron gauge (MKS) measured the total pressure of the chamber. A closed loop control PEM system allowed to control the oxygen flow rate by the measurement of the optical intensity of the 391.91 nm lanthanum emission line ( $I_{La^*}$ ) collected through an optical fiber. The signal is sent to a spectrometer

(Ropper Scientific SpectraPro 500i), with a 1200 groove mm<sup>-2</sup> grating and a photomultiplier tube (Hamamatsu R 636). A homemade software developed with Labview® managed the information and control the oxygen flow rate to keep the intensity of the optical signal  $I_{La^*}$  at the desired value.

### 2.2. Structural, morphological

Samples were analyzed by Scanning Electron Microscopy (SEM) using a JEOL JSM 7800 F to determine their microstructure. Metallic ratios were measured by Energy Dispersive Spectroscopy (EDS). Samples were coated with carbon by evaporation under vacuum before EDS analyses. These analyses were performed at Working Distance equal 10 mm with 15 kV acceleration voltage and 2 nA probe current. 5 measurements were made on different parts of the sample and an average value was calculated. A BRUKER D8 focus diffractometer was used to check the structural features of the samples. This device, equipped with the LynxEye linear detector, use the K<sub>α1</sub> + α<sub>2</sub> of cobalt radiations to XRD collect patterns. Analyses were performed at room temperature from 20° to 80° scattering angle by steps of 0.019°. The thickness of coatings was measured on glass slides with an Altisurf profilometer (Altimet) allowing an accuracy of 20 nm. This device was calibrated before each measurement following the CETIM accreditation (reference sample number 787569). Measurements were performed using the "step" method in which a small surface tape is stuck prior to deposition process, then removed leaving a step revealing the thickness of films.

### 2.3. Electrical measurements

The electrical resistivity measurements were performed with a HP 3458 A multimeter on La Ni O films deposited on alumina substrates. With regard to its high insulating character, it is assumed in the following that the substrate has no significant contribution to the electrical conductivity. The four point probe technique with four Pt aligned electrodes was used. Two outer probes behaved as the current carrying electrodes (I1, I2) and the two inner ones were used to measure the voltage (E1, E2). Two cell configurations were used for the measurements: cell 1 was used to define the resistivity at room temperature (Jandel, Linslade, UK). It is a standard and certified cell allowing the accurate determination of the geometric factor. The second cell developed by the LEPMI laboratory (Grenoble, France) allows measurements at various temperatures. This latter cell is placed inside an alumina tube and positioned into a furnace (Pekly, Thions Gardais, France). The

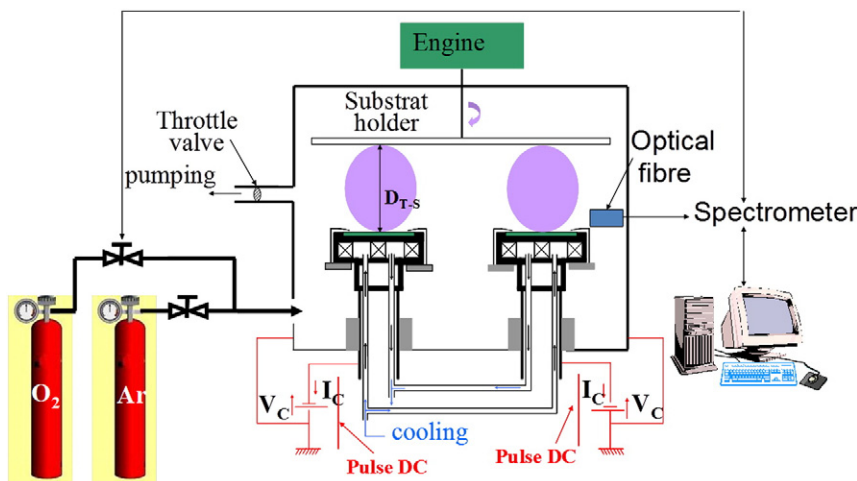


Fig. 1. Scheme of the deposition setup.

comparison of the resistance measured at room temperature with cell 1 ( $R_1$ ) and cell 2 ( $R_2$ ) was used to determine the geometric factor of cell 2 thanks to the relationship (Eq. (1)):

$$\sigma = \frac{1}{\rho} \frac{1}{4.381 \cdot \frac{R_2}{R_1} \cdot t} \quad (1)$$

where 4.381 is the correction factor calculated from the diameter of the sample ( $\varnothing = 16$  mm) and  $t$ , the thickness of the film.

#### 2.4. Complete cell tests

The samples were inserted into a homemade cell designed at the ICMCB laboratory (Bordeaux, France). A nickel/gold grid was maintained on the cathode side with springs. Before cell tests, the cathode layer of the stack was first crystallized at 1073 K during 10 h. Anode layer was then reduced at 973 K during 6 h. Measurements were performed at 973 K with 120 mL/min of  $H_2 + 3 \text{ vol.}\% H_2O$  on the anode side and 240 mL/min air on the cathode side. Electrochemical measurements are realized by the use of an Autolab PGSTAT30 potentiostat driven by GPES and FRA software for voltammetry and impedance measurements. In cyclic voltammetry, the output current is measured from different potentials. The parameters for the Voltammetry measurements were 2 s equilibrium time, start potential at OCV, end potential 0.2 V and 5 mV/s speed. Electrochemical Impedance Spectroscopy (EIS) was then performed on the Open Circuit Voltage (OCV) from 100 mHz to 10 MHz with 10 points per decade with 50 mV amplitude.

### 3. Result and discussion

#### 3.1. Deposition of the cathode layer

##### 3.1.1. Determination of the optimal regulation setpoint for each pressure

Fig. 2 shows the discharge voltage versus oxygen flow rate curves of La and Ni targets during their sputtering at discharge current values respectively 2.5 and 0.7 A applied to metallic targets. For the nickel material, the target voltage oxygen flow rate curve is reversible which corresponds to so called stable sputtering conditions. For the lanthanum metallic target, an hysteresis loop characteristic of the instability of the La-O system is observed, depending on whether oxygen flow rate increases or decreases. With magnetron sputtering technique, the use of metallic targets in presence of oxygen can lead to the deposition of ceramic or metallic coatings depending on the oxygen content. Low oxygen flow rates are associated with high sputtering rate but the coating is often oxygen deficient (metallic mode). Conversely, high oxygen flow rates induce a contamination of the target's surface (i.e. formation

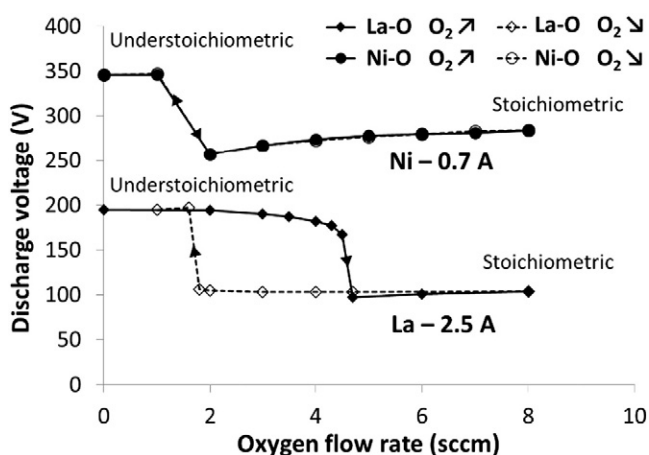


Fig. 2. Stability of the La-O and Ni-O systems at a pressure of 1.9 Pa.

of oxide compounds). When the surface of the target is entirely oxidized (poisoned mode), the sputtering rate decreases and stoichiometric oxides are deposited. The physicochemical state that conditions the average sputtering yield of the target, is usually a monotonic and quite proportional function of the optical signal  $I_M^*$  measured by Optical Emission Spectroscopy [26-27]. The PEM system allows the deposition of coatings in the unstable domain of the hysteresis loop by fixing the intensity of the plasma emission line of the target using a closed loop control of the oxygen flow rate as explained in a previous work [23]. In deed, PEM is a very suitable technique to allow high rate growth of oxide coatings [20,28] under unstable sputtering conditions (transition mode). The PEM control was then performed on the La target with a fixed discharge current of 2.5 A.

Fig. 3 presents the evolution of the 394.91 nm emission line intensity vs. oxygen flow rate at total pressures varying from 0.4 to 4.8 Pa. Working pressures of 0.4 and 1.9 Pa are obtained by increasing the argon flow rate from 50 to 200 sccm with the highest pumping speed. Working pressures of 3.2 and 4.8 Pa are obtained by throttling the suction pipe and also by increasing the argon flow rate from 50 to 200 sccm. Stable sputtering conditions, represented by full symbols, are obtained by fixing different oxygen flow rates while unstable sputtering conditions, pointed by open symbols, are collected by using the PEM system to maintain the optical intensity at different values. With pure argon, the optical intensity is maximal and fixed at 100%. When increasing oxygen flow rate, optical emission slightly decreases due to the target poisoning. A drop of the optical emission until about 5%, occurs at critical oxygen flow rate. This critical oxygen flow rate evolves from about 6.4 to 2.6 sccm  $O_2$  with increasing argon pressure from 0.4 to 4.8 Pa which is consistent with a decrease of the pumping speed and a stronger diffusion of sputtered metal atoms. Whatever the total pressure, using PEM allows the deposition with an optical intensity set point ( $S$ ) located in the unstable domain inside the hysteresis loop and allows the deposition of oxide coatings with higher deposition rates. The setpoint  $I_{La}^*$  is fixed by the operator, allowing the control of the oxygen flow rate by the software. The  $S$  value was varied from 95 to 10% to obtain the plotted open symbols (Fig. 3) in the unstable domain. The Table 1 summarizes the evolution of the hysteresis domain as function of the total pressure. In a previous work [20], the methodology for determining the regulation set point had been already described on the La-O system. In this study, the regulation set point is respectively 55%, 65%, 70% and 80% for 0.4, 1.9, 3.2 and 4.8 Pa.

##### 3.1.2. Deposition of La-Ni-O coatings: influence of total pressure

The coatings are deposited by co-sputtering of La and Ni metallic targets in Ar- $O_2$  mixtures for which the oxygen flow rate is controlled by the PEM system. Fig. 4 presents the metallic La/Ni atomic ratio

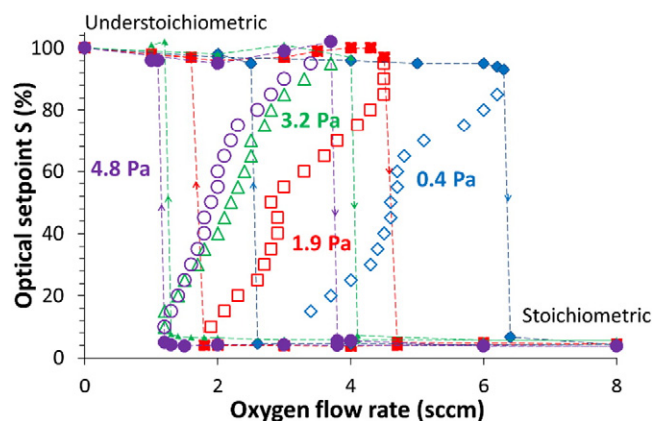


Fig. 3. Influence of the pressure on the instability of sputtering conditions. Hysteresis loop oxygen flow rate vs. 395 nm La emission line intensity. Stable sputtering conditions (full symbols) and unstable sputtering conditions by PEM (open symbols).

**Table 1**  
Evolution of the hysteresis domain with the total pressure.

| Total pressure (Pa) | Oxygen flow rate to ESM → RSM (sccm) | Oxygen flow rate to RSM → ESM (sccm) | Width hysteresis (sccm) |
|---------------------|--------------------------------------|--------------------------------------|-------------------------|
| 0.4                 | 6.4                                  | 2.5                                  | 3.9                     |
| 1.9                 | 4.7                                  | 1.8                                  | 2.9                     |
| 3.2                 | 4.1                                  | 1.3                                  | 2.8                     |
| 4.8                 | 3.8                                  | 1.2                                  | 2.6                     |

determined by EDS analyses versus the discharge current applied to the Ni target while the La target current is fixed at 2.5 A. For each pressure, the metallic ratio La/Ni decreases linearly with increasing the discharge current on the Ni target. The current on the Ni target necessary to obtain the targeted composition for  $\text{La}_2\text{NiO}_4$  also increases with increasing the total pressure. This should be ascribed to a stronger diffusion of Ni than La in the gas phase due to its lower mass. Optimal discharge current of 0.38 A, 0.44 A, 0.57 A and 0.68 A with PEM set points fixed at 55%, 65%, 70% and 80% for 0.4, 1.9, 3.2 and 4.8 Pa respectively were determined to obtain the  $\text{La}_2\text{NiO}_4$  composition. In fact, as EDS analyses do not allow a reliable determination of the oxygen content into the coatings, it was only used to estimate the metallic composition.

As expected for each pressure, XRD measurements performed on as deposited samples show the presence of an amorphous structure whatever the composition of the coating. In order to crystallize the  $\text{La}_2\text{NiO}_4$  phase, annealing at 1173 K for 2 h were applied according to a previous study [20] with samples presenting a La/Ni ratio of about 2. Fig. 5 presents the XRD patterns of annealed coatings deposited on alumina substrates at 1173 K for 2 h for the different total pressures with a La/Ni ratio close to 2. The increase of the partial pressure changes the phase content of the coating according to the slight drift of the coating composition. For these experimental conditions, high pressure favors the formation of La Ni O perovskite phases ( $\text{La}_4\text{Ni}_3\text{O}_{10}$  and/or  $\text{La}_3\text{Ni}_2\text{O}_7$ ) and lanthanum oxide in addition to  $\text{La}_2\text{NiO}_4$  desired structure for a La/Ni ratio close to 2. These perovskite phases are normally formed when the La/Ni ratio is lower, but the  $\text{La}_2\text{O}_3$  compound, which should be formed at higher ratio, is present. The occurrence of  $\text{La}_4\text{Ni}_3\text{O}_{10}$  together with  $\text{La}_2\text{NiO}_4$  and  $\text{La}_2\text{O}_3$  was already observed with high oxygen partial pressures by others [29] and could explain our results at 1.9 and 4.8 Pa. The intensity of lanthanum oxide peak after deposition at 3.2 and 4.8 Pa is consistent with the slight excess of La (La/Ni =  $2.12 \pm 0.10$  and  $2.16 \pm 0.04$  at 3.2 and 4.8 Pa respectively). Intensity of  $\text{La}_2\text{O}_3$  peak is higher at 4.8 Pa because high amount of nickel is present in  $\text{La}_4\text{Ni}_3\text{O}_{10}$  and/or  $\text{La}_3\text{Ni}_2\text{O}_7$  structures. It also could be ascribed either to a gradient of composition in the thickness of the coating or more probably to a

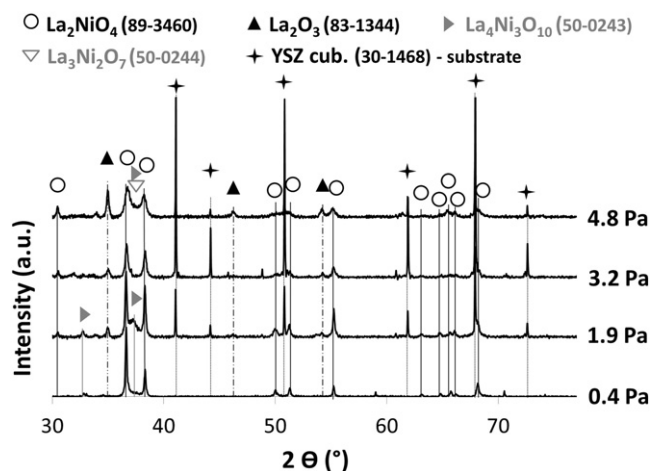


**Fig. 5.** XRD spectra as a function of total pressure after annealing at 1173 K for 2 h.

gradient in the width of the columns, the external surface of the columns being probably depleted in Ni, which should also explain the quite large amount of  $\text{La}_2\text{O}_3$  in the coatings deposited at high pressure which also develop the higher specific surface area.

### 3.1.3. Deposition of cathode layer with porosity gradient

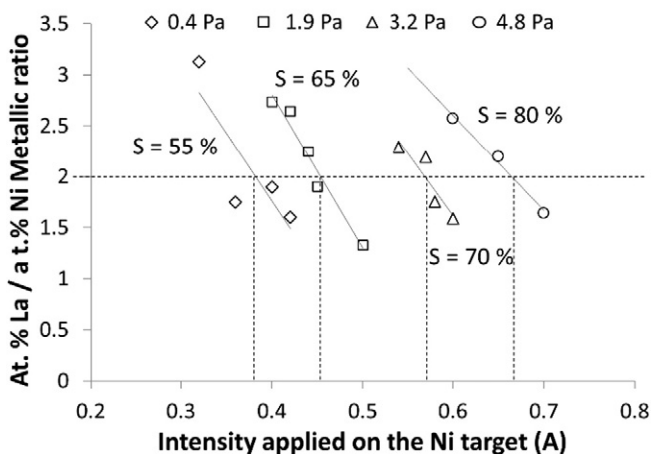
Previous studies have shown that dense coatings deposited at low pressure (0.4 Pa) reproduce the morphology of alumina and YSZ substrates [20]. According to the Thornton's diagram revised by Anders [30], the morphology becomes less and less dense with decreasing the average energy of impinging species, e.g. by increasing the deposition pressure (Fig. 6a, b). Porous morphology is then expected to increase the exchange surface between the cathode and the gas phase. Nevertheless, the adhesion of porous coatings seems to be low. From the literature, the use of a thin and dense interfacial cathode layer is supposed to improve the adhesion of the cathode by increasing the contact between the porous cathode and electrolyte layer [31]. For all these reasons, it was decided to deposit a cathode with porosity gradient with a general La/Ni ratio of about 2 by increasing the pressure during the deposition stage according to the results presented earlier. YSZ pellets and Ni YSZ/YSZ/GDC commercial anode supported half cells were then covered by a gradient cathode coating. Table 2 summarizes the deposition parameters of those coatings. EDS measurements performed on the top of these as deposited and annealed samples confirmed a La/Ni ratio close to 2 ( $1.87 \pm 0.04$  and  $1.95 \pm 0.05$  for as deposited and annealed coatings respectively).

Fig. 6c and d present the morphology of the coating deposited on YSZ pellet after annealing at 1173 K during 2 h from top view and cross section respectively. The desired morphology is obtained on this sample. The top view shows an island like growth of the gradient coating with cracks like separations of the islands corresponding coarsely to the size of the YSZ grains and expected to contribute to the increase of surface exchange between the gas phase and the cathode material.

## 3.2. Electrical and electrochemical tests

### 3.2.1. Electrical analyses

In order to assess the characteristics of the well crystallized films, electrical measurements were performed implementing a four point probe method on annealed samples. It is compared with the literature data [6,8,33] and with dense cathode layers presented in a previous paper [20]. Fig. 7 highlights that, despite a lower conductivity at room temperature of the gradient cathode, its conductivity around 973–1073 K ( $30-60 \text{ S}\cdot\text{cm}$ ) is closed to that of bulk cathodes of the literature.



**Fig. 4.** Evolution of atomic composition ratio La/Ni measured by EDS as a function of current dissipated on the Ni target ( $I_{\text{La}} = 2.5 \text{ A}$ ) at different total pressures.

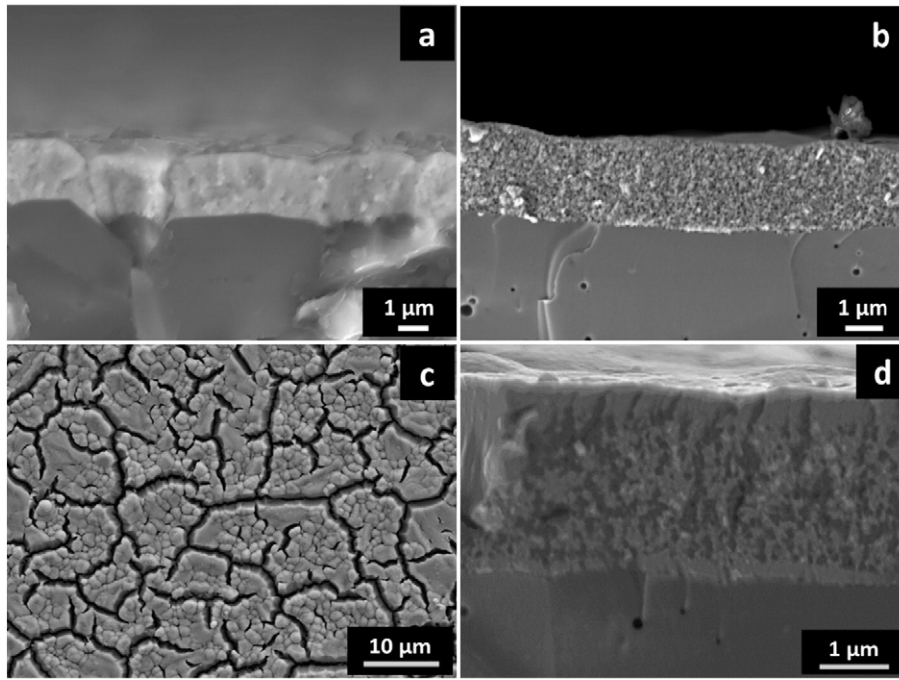


**Fig. 6.** SEM micrographs of LNO coatings deposited on YSZ substrates after annealing at 1173 K for 2 h. Brittle fracture cross section of samples deposited at 0.4 Pa (a), and at 4.8 Pa (b). Top view (c) and brittle cross section (d) of the porosity gradient coatings.

### 3.2.2. Complete cell tests

Previous studies proved that either air or nitrogen conditions gas crystallization treatments were not suitable for this last step of the complete cell elaboration. Indeed, air conditions treatment at 1173 K deteriorated the anodic side of the cell and nitrogen conditions did not allow the targeted lanthanum nickelate phase. Thus, cathode materials were crystallized prior to the test in the single cell test setup to obtain the convenient  $\text{La}_2\text{NiO}_4$  structure. It was performed by increasing the cell temperature up to 1073 K for 6.5 h by introducing on the cathode side 120 sccm  $\text{O}_2$  and on the anode side a 6 sccm humidified  $\text{H}_2$  114 sccm  $\text{N}_2$  gas mixture. Fig. 8 presents structure comparison of Ni/YSZ/YSZ/GDC cells covered with the porosity gradient LNO layer (p LNO) and with a dense LNO layer produced at 0.4 Pa (d LNO). Due to a thin cathode layer, GDC substrate's structure is identified. As deposited samples are amorphous. XRD measurements of the crystallized coatings identify the same structure of these samples. The same tetragonal lanthanum nickelate phase is identified with a very low amount of lanthanum oxide impurities. These analyses prove that the crystallization method is suitable in these conditions to crystallize the targeted phase without major impurities.

The anode reduction was then performed at 973 K with a gas flow evolving linearly from 6 to 120 sccm of humidified  $\text{H}_2$  on the anode side while 120 sccm  $\text{O}_2$  was injected on the cathode side. The Open Circuit Voltage (OCV) was measured during the reduction stage (Fig. 9). The shape of the reduction curves is quite similar for p LNO and d LNO cells. Maximal OCV values were measured at 0.9 V for both cells. This value is quite lower to the theoretical value of 1.05 V at this

temperature and proves that it depends mostly on the electrolyte tightness. Increasing oxygen flow rate has no significant effect on the cell's OCV.

When, the OCV is stable, complete cells tests begin. Fig. 10 presents voltammetry tests of these complete cells at 973 K to target the IT SOFC's application domain. These measurements indicate a maximum power density of 71 and 51  $\text{mW}/\text{cm}^2$  for porous and dense cathodes, respectively. It increases up to about 140  $\text{mW}/\text{cm}^2$  for the porous cathode when the test is performed at 1073 K. In the literature, anode supported cells with electrolyte manufactured by reactive magnetron sputtering process (RMS) reach a power density of 410  $\text{mW}/\text{cm}^2$  at 973 K [32] and 600  $\text{mW}/\text{cm}^2$  at 1073 K [33]. Nevertheless, no complete cells presenting cathode manufactured by RMS were analyzed in complete cell tests. Some improvements of the cell microstructure and reduction of the thickness have to be performed in order to obtain higher performances. These results prove that the porosity gradient is an efficient

**Table 2**  
deposition conditions of the coating with porosity gradient.

| Total pressure (Pa)           | 0.4     | 1.9     | 3.2     | 4.8     |
|-------------------------------|---------|---------|---------|---------|
| Set point (%)                 | 55      | 65      | 70      | 80      |
| $\text{O}_2$ flow rate (sccm) | 5.0     | 4.3     | 3.6     | 3.3/3.4 |
| Run duration (min)            | 15      | 30      | 50      | 100     |
| $I_{\text{La}}$ (A/kHz)       |         |         | 2.5/50  |         |
| $I_{\text{Ni}}$ (A/kHz)       | 0.38/50 | 0.44/50 | 0.57/50 | 0.67/50 |

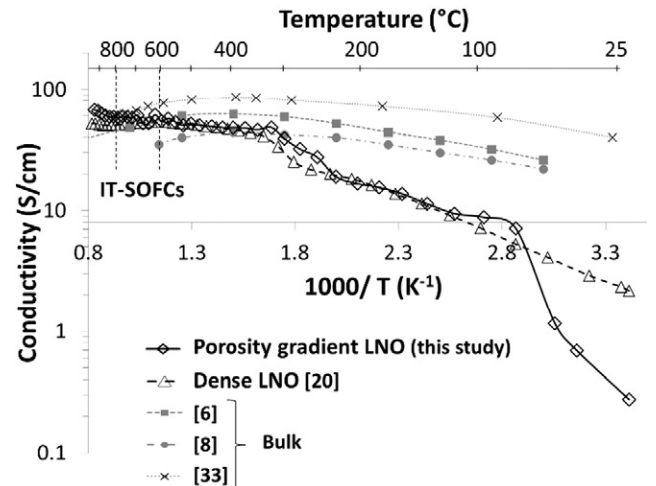


**Fig. 7.** Conductivity of porosity gradient coating previously annealed at 1173 K for 2 h measured as a function of annealing temperature compared with literature results.

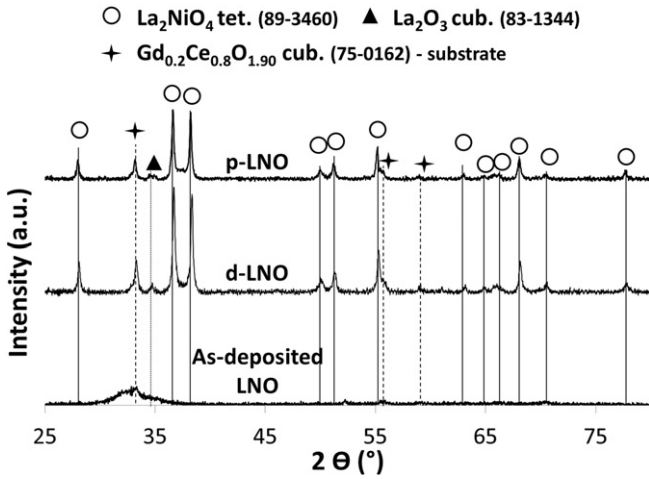


Fig. 8. XRD measurements of p-LNO and d-LNO complete cells as-deposited and after tests.

way to improve the performances of the cell. Indeed, despite the performances are in the same order of magnitude, power densities are improved to 28% by replacing dense cathode by a more porous one. Cathode microstructure should also play an important role in the performances of the cells. This may increase the oxygen reactive area.

To explain the rather low performances of the cells (71 and 51  $\text{mW}/\text{cm}^2$  for porous and dense cathodes), Electrochemical Impedance Spectroscopy (EIS) characterizations were performed on these samples. Impedance of a circuit presents real ( $Z'$ ) and imaginary ( $Z''$ ) parts as shown in (Eq. (2)).

$$Z(\omega) = \text{Re}(Z) + j\text{Im}(Z) = Z' + jZ'' \quad (2)$$

Impedance is usually represented in complex plan of Nyquist from the relation (Eq. (3)).

$$-Z'' = f(Z') \quad (3)$$

Fig. 11 presents Nyquist plots of the complete cells under OCV. These diagrams were fitted using Z View software. Modeled data are represented by lines in the figures while experimental measurements are represented by points. Four contributions characteristic of different phenomena appearing were identified in high, medium and low

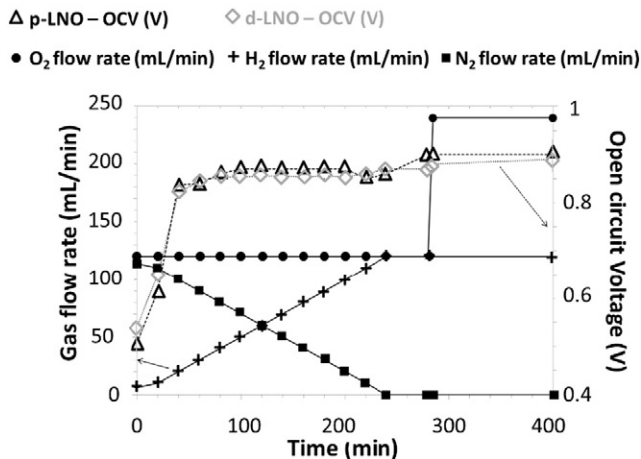


Fig. 9. Evolution of p-LNO and d-LNO complete cells' Open circuit Voltage (OCV) during reduction of anode layer at 973 K.

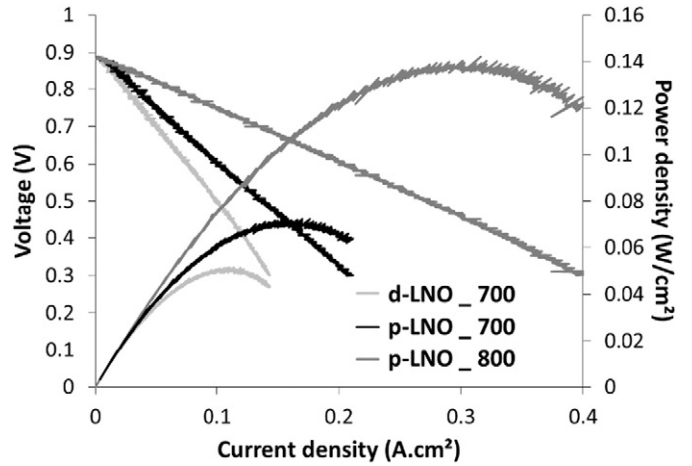


Fig. 10. Voltammetry tests of p-LNO and d-LNO complete cells at different temperatures.

frequency ranges. Each contribution can be modeled by a sum of elementary circuits (resistance, capacitance, and inductance). Constant Phase Element function (CPE) can be used to better fit the experiments values. This function can act as a resistance, capacitance or inductance and is more and more used with electrochemical phenomena. Resistance and associated capacitance values were extracted from these fits. Nyquist curves were fitted by the same equivalent circuits. Their shapes are similar, only the different resistances varying. Total resistance of the "p LNO" sample is lower than that of the "d LNO" sample, explaining performances measured on the different samples (Fig. 9). These resistances remain very high and explain the lower output power densities of the cells compared to literature data (71  $\text{mW}/\text{cm}^2$  and 600  $\text{mW}/\text{cm}^2$  respectively). The resistance at high frequencies (serial resistance), usually depending on the electrolyte resistance, remains identical for both since the electrolyte coatings were deposited during a same run. The characteristics attributed for medium or low frequencies underline the different electrochemical phenomena occurrence on these samples. Using the Schouler method [34], resistance and CPE are each assigned to the resistance and capacitance that can be correlated to a specific electrochemical process. On the basis of the fitted data, the equivalent capacitance and the frequency relaxation of each contribution were calculated using relations (Eqs. (4) and (5)).

$$C_{eq} = \text{Re} \left( \frac{1}{n} \right) * C^{\frac{1}{n}} \quad (4)$$

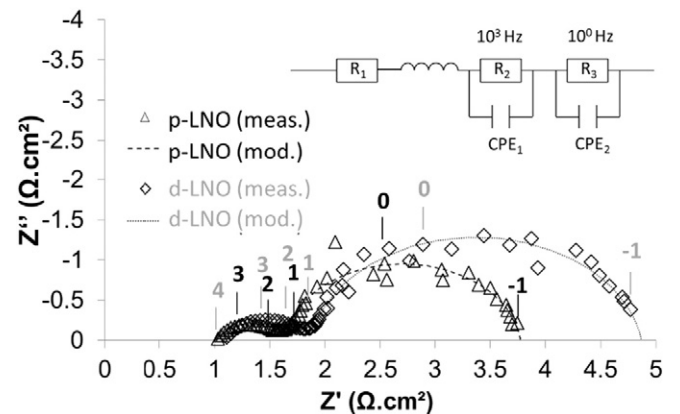


Fig. 11. Nyquist plots of p-LNO and d-LNO complete cells. Models are represented by lines. Experimental results are represented by symbols. Logarithm of frequency are indicated in the figure.

**Table 3**

Parameters determined by electrochemical impedance spectroscopy.

| Domain       | Phenomena                                 | p-LNO               | d-LNO               |
|--------------|---|---------------------|---------------------|
| HF           | $R_1 (\Omega \cdot \text{cm}^2)$          | 1.01                | 1.08                |
|              | $R_2 (\Omega \cdot \text{cm}^2)$          | 0.63                | 0.79                |
| MF           | $C_{eq2} (\text{F} \cdot \text{cm}^{-2})$ | $8.1 \cdot 10^{-4}$ | $6.9 \cdot 10^{-4}$ |
|              | $f_2 (\text{Hz})$                         | $2.3 \cdot 10^4$    | $3.2 \cdot 10^4$    |
|              | $R_3 (\Omega \cdot \text{cm}^2)$          | 2.12                | 2.99                |
| LF           | $C_{eq3} (\text{F} \cdot \text{cm}^{-2})$ | $4.0 \cdot 10^{-1}$ | $3.0 \cdot 10^{-1}$ |
|              | $f_3 (\text{Hz})$                         | $1.2 \cdot 10^0$    | $8.8 \cdot 10^{-1}$ |
| MF + LF      | $R_p (\Omega \cdot \text{cm}^2)$          | 2.75                | 3.78                |
| HF + MF + LF | ASR ( $\Omega \cdot \text{cm}^2$ )        | 3.76                | 4.86                |

with R: electrical resistance, n: decentering angle of the Constant Phase Element function, C: capacitance of the phenomenon.

$$f_n = \frac{1}{2\pi(C_{eq_n} R_n)^{\frac{1}{n}}} \quad (5)$$

Table 3 presents the parameters of the different phenomena for each sample. High, Medium and Low frequency phenomenon are named by 1 ( $R_1$ ,  $C_{eq1}$ ,  $f_1$ ) and 2 ( $R_2$ ,  $C_{eq2}$ ,  $f_2$ ) and 3 ( $R_3$ ,  $C_{eq3}$ ,  $f_3$ ) respectively. Polarization Resistance ( $R_p$ ) is calculated by the sum of  $R_2$  and  $R_3$ . ASR represents the complete cell resistance. Complete cell resistance ASR are much higher than requirements for IT SOFCs (i.e.  $0.8 \Omega \cdot \text{cm}^2$ ). These high values explain the poor performances obtained with these cells at 973 K. Numerous limitations should be induced by the use of several layers. The compatibility of these materials and structures has to be optimized in order to improve the performances by decreasing resistances. The low frequency range (LF) is characterized by high capacitance values,  $C_{eq} \approx 1 \cdot 10^{-1} \text{ F} \cdot \text{cm}^{-2}$  [11,35], and it was identified as the result of gaseous diffusion through the electrode. The capacitance of the medium frequency contribution (MF) is found to be larger,  $C_{eq} \approx 10^{-3} \cdot 10^{-1} \text{ F} \cdot \text{cm}^{-2}$ . The source of this contribution is more complicated to identify; it has been assigned as Oxygen Reduction Reaction (ORR) occurring at the electrode/gas interface in literature [11,3] or ionic transfers at the electrode/electrolyte interface [8].

Because cathode material is the only variable parameter, polarization resistance should be due to the cathode layer. Equivalent capacitances and relaxation frequencies are close ( $10^{-3} \text{ F} \cdot \text{cm}^{-2}$ ,  $10^4 \text{ Hz}$  and  $0.1 \text{ F} \cdot \text{cm}^{-2}$ ,  $1 \text{ Hz}$  for the MF and LF phenomena respectively). These values indicate that same electrochemical processes happen. Resistance values of the MF and LF phenomena are significantly improved by this new cathode architecture (20% and 30% gain for MF and LF phenomena respectively). The most important gain happens at LF, corresponding to gaseous diffusion through cathode layer. This indicates the realization of coating with higher porosity. From these two contributions at MF and LF, an electrode polarization resistance of 3.75 and 2.78  $\Omega/\text{cm}^2$  was determined for “d LNO” and “p LNO” respectively. Nevertheless, the specifications of fuel cell electrodes have to be lower than  $0.5 \Omega/\text{cm}^2$ . The high resistances obtained on samples are too high because of not optimized morphology even if making a porosity gradient thin cathode seems to be a promising option. Analyses of structures and microstructures of cathode and electrolyte/cathode interface were then performed to point differences between samples and to explain results. Fig. 12 shows SEM observations of surface (a) and the brittle cross section (b, c, d) of the complete cell after electrical tests. Surface condition of every sample is not completely smooth because of the anode substrate morphology and the high pressure during the last step of the cathode deposition. Interface between the GDC interlayer and the cathode layer is improved in the “p LNO” sample (Fig. 12c) in comparison with the “d LNO” cathode (Fig. 12d). This can explain the best resistance at medium frequencies (20%) noticed with EIS characterization. It is then obvious that the p LNO coating is less tight than the d LNO coating. It facilitates the oxygen permeation through the cathode layer and should explain the lower resistance (30%) at low frequencies. No differences can be pointed between d LNO and p LNO samples at low magnification in spite of predicted microstructures. Indeed, “island shape” areas are in minority on the surface. Most of the surface is not modified. This fact should explain the poor performances obtain because active surface is smaller than wished. A combination of lower temperatures with pressure could explain the different microstructures. Higher magnification permits to underline differences between the two cathodes (Fig. 12c and d). Interface between the GDC layer and the cathode layer is improved in the “p LNO” sample.

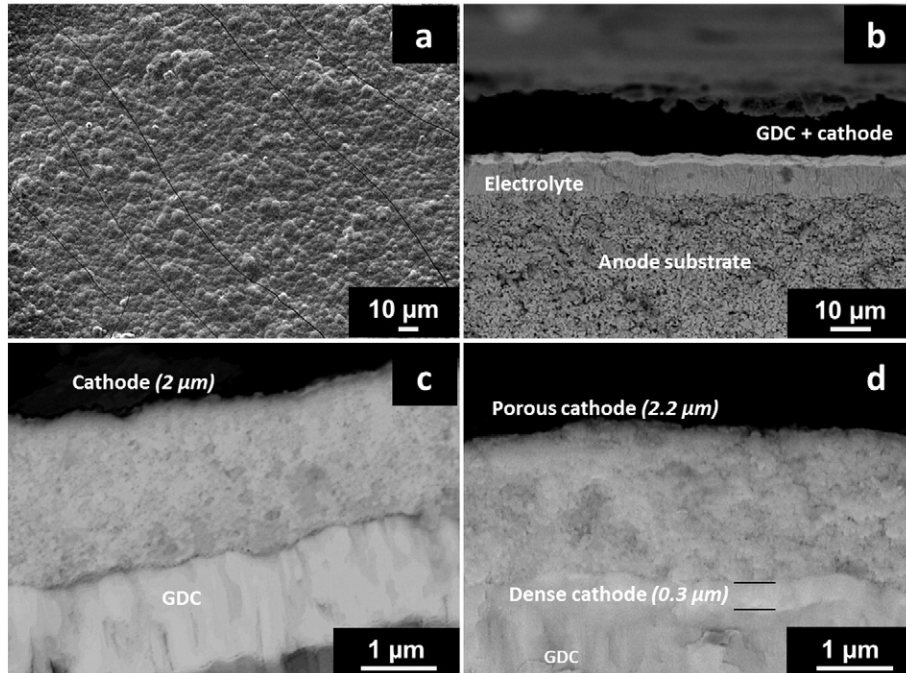


Fig. 12. SEM view of surface (a) and brittle fracture cross section complete cells with p-LNO (b, c) and d-LNO (d) cathode after electrical tests with different magnifications.

## 4. Conclusion

A porosity gradient La-Ni-O coating was deposited by co-sputtering of La and Ni metallic targets in the presence of reactive argon-oxygen gas mixtures using Plasma Emission Monitoring by gradually increasing the pressure during the deposition stage. Increasing the pressure induces the decrease of the unstable domain width and change the optimal sputtering conditions to obtain  $\text{La}_2\text{NiO}_4$  structure (regulation setpoint and current on nickel target). Moreover, higher total pressure change the phase occurrence and allows the presence of both  $\text{La}_2\text{O}_3$  and  $\text{La}_3\text{Ni}_2\text{O}_7$  and  $\text{La}_2\text{NiO}_4$  phases, resulted by a possible increase of resistance. Increasing the pressure also leads to an increase of the porosity of the coatings until obtaining “island shape” of crystallized coatings. Four-point probe measurements show the interesting electrical behavior in IT-SOFCs utilization domain of porosity gradient cathode coatings. Ni-YSZ/YSZ/GDC/LNO complete cells were then built using dense LNO and gradient cathode LNO and were tested in a cell bench. In order to avoid the deterioration of the cell's component, the crystallization of the cathode and the reduction of the anode were performed during the complete cell tests, allowing to obtain the convenient  $\text{La}_2\text{NiO}_4$  structure. Nevertheless, the performances are lower than expected with those materials. Impedance measurements allow to point the reasons of these low performances ( $71 \text{ mW/cm}^2$ ), each layer of the cell presents high resistance but the most important remains the cathode where polarization resistance is three times higher than that of the electrolyte. Nevertheless, it is also shown that the use of a porosity gradient cathode is the convenient way to improve the cell performance. The low performances are certainly induced by the cathode thickness, in future work, it should be developed cathode architected with thickness greater than  $2.5 \mu\text{m}$ .

## Acknowledgments

The authors thank the Pays de Montbéliard Agglomération (n°13/083) for their financial support during this study.

## References

- [1] F. Tietz, V.A.C. Haanappel, A. Mai, J. Mertens, D. Stöver, Performance of LSCF cathodes in cell test, *J. Power Sources* 156 (2006) 20–22.
- [2] J. Pena-Martinez, D. Marrero-Lopez, D. Pérez-Coll, J.C. Ruiz-Morales, P. Nunez, Performance of XScOF (X = Ba, La and Sm) and LSCrX' (X' = Mn, Fe and Al) perovskite-structure materials on LSGM electrolyte for IT-SOFC, *Electrochim. Acta* 52 (2007) 2950–2958.
- [3] K.K. Hansen, K. Vels Hansen, A-site deficient  $(\text{La}_{0.6}\text{Sr}_{0.4})_{1-x}\text{Fe}_{0.8}\text{Co}_{0.2}\text{O}_{3-\delta}$  perovskites as SOFC cathodes, *Solid State Ionics* 178 (2007) 1379–1384.
- [4] K.T. Lee, A. Manthiram, Comparison of  $\text{Ln}_{0.6}\text{Sr}_{0.4}\text{CoO}_{3-\delta}$  (Ln = La, Pr, Nd, Sm, and Gd) as Cathode Materials for Intermediate Temperature Solid Oxide Fuel Cells, *J. Electrochem. Soc.* 153 (2006) 794–798.
- [5] J.-C. Chang, M.-C. Lee, R.-J. Yang, Y.-C. Chang, T.-N. Lin, C.-H. Wang, W.-X. Kao, L.-S. Lee, Fabrication and characterization of  $\text{Sm}_{0.2}\text{Ce}_{0.8}\text{O}_{2-\delta}$ - $\text{Sm}_{0.5}\text{Sr}_{0.5}\text{CoO}_{3-\delta}$  composite cathode for anode supported solid oxide fuel cell, *J. Power Sources* 196 (2011) 3129–3133.
- [6] E. Boehm, J.-M. Bassat, P. Dordor, F. Mauvy, J.-C. Grenier, P. Stevens, Oxygen diffusion and transport properties in non-stoichiometric  $\text{Ln}_{2-x}\text{NiO}_{4+\delta}$  oxides, *Solid State Ionics* 176 (2005) 2717–2725.
- [7] V.V. Khariton, E.V. Tsipis, E.N. Naumovich, A. Thursfield, M.V. Patrakee, V.A. Kolotygin, J.C. Waerenborgh, I.S. Metcalfe, Mixed conductivity, oxygen permeability and redox behavior of  $\text{K}_2\text{NiF}_4$ -type  $\text{La}_2\text{Ni}_{0.9}\text{Fe}_{0.1}\text{O}_{4+\delta}$ , *J. Solid State Chem.* 181 (2008) 1425–1433.
- [8] J. Dailly, S. Fourcade, A. Largeteau, F. Mauvy, J.C. Grenier, M. Marrony, Perovskite and  $\text{A}_2\text{MO}_4$ -type oxides as new cathode materials for protonic solid oxide fuel cells, *Electrochim. Acta* 55 (2010) 5847–5853.
- [9] R. Sayers, R.A. De Souza, J.A. Kilner, S.J. Skinner, Low temperature diffusion and oxygen stoichiometry in lanthanum nickelate, *Solid State Ionics* 181 (2010) 386–391.
- [10] H. Zhao, F. Mauvy, C. Lalanne, J.-M. Bassat, S. Fourcade, J.-C. Grenier, New cathode materials for IT-SOFC: phase stability, oxygen exchange and cathode properties of  $\text{La}_{2-x}\text{NiO}_{4+\delta}$ , *Solid State Ionics* 179 (2008) 2000–2005.
- [11] B. Philippeau, F. Mauvy, C. Matazaud, S. Fourcade, J.-C. Grenier, Comparative study of electrochemical properties of mixed conducting  $\text{Ln}_2\text{NiO}_{4+\delta}$  (Ln = La, Pr and Nd) and  $\text{La}_{0.6}\text{Sr}_{0.4}\text{Fe}_{0.8}\text{Co}_{0.2}\text{O}_{3-\delta}$  as SOFC cathodes associated to  $\text{Ce}_{0.9}\text{Gd}_{0.1}\text{O}_{2-\delta}$ ,  $\text{La}_{0.8}\text{Sr}_{0.2}\text{Ga}_{0.8}\text{Mg}_{0.2}\text{O}_{3-\delta}$  and  $\text{La}_9\text{Sr}_1\text{Si}_6\text{O}_{26.5}$  electrolytes, *Solid State Ionics* 249–250 (2013) 17–25.
- [12] K. Zhao, Y.-P. Wang, M. Chen, Q. Xu, B.-H. Kim, D.-P. Huang, Electrochemical evaluation of  $\text{La}_2\text{NiO}_{4+\delta}$  as a cathode material for intermediate temperature solid oxide fuel cells, *Int. J. Hydrog. Energy* 39 (2014) 7120–7130.
- [13] I. Garbayo, V. Esposito, S. Sanna, A. Morata, D. Pla, L. Fonseca, N. Sabaté, A. Taron, Porous  $\text{La}_{0.6}\text{Sr}_{0.4}\text{CoO}_{3-\delta}$  thin film cathodes for large area micro solid oxide fuel cell power generators, *J. Power Sources* 248 (2014) 1042–1049.
- [14] H.-S. Noh, K.J. Yoon, B.-K. Kim, H.-J. Je, H.-W. Lee, J.-H. Lee, J.-W. Son, The potential and challenges of thin-film electrolyte and nanostructured electrode for yttria-stabilized zirconia-base anode-supported solid oxide fuel cells, *J. Power Sources* 247 (2014) 105–111.
- [15] T. Mukai, S. Tsukui, K. Yoshida, M. Adachi, K. Goretta, Influence of thin films structure of  $\text{Gd}_{0.5}\text{Sr}_{0.5}\text{CoO}_3$  cathode on impedance spectroscopy, *Electrochem. Soc. Trans.* 57 (2013) 1885–1891.
- [16] P. Briois, A. Billard, A comparison of electrical properties of sputter-deposited electrolyte coatings dedicated to intermediate temperature solid oxide fuel cells, *Surf. Coat. Technol.* 201 (2006) 1328–1334.
- [17] N. Jordan, V. Assenmacher, S. Uhlenbruck, V.A.C. Haanappel, H.P. Buchkremer, D. Stöver, W. Mader,  $\text{Ce}_{0.8}\text{Gd}_{0.2}\text{O}_{2-\delta}$  protecting layers manufactured by physical vapor deposition for IT-SOFC, *Solid State Ionics* 179 (2008) 919–923.
- [18] A.A. Solov'yev, N.S. Sochugov, S.V. Rabortkin, A.V. Shipoliva, I.V. Ionov, A.N. Kovalchuk, A.O. Borduleva, Application of PVD methods to solid oxide fuel cells, *Appl. Surf. Sci.* 310 (2014) 272–277.
- [19] P. Briois, F. Perry, A. Billard, Structural and electrical characterisation of lanthanum nickelate reactively sputter-deposited thin films, *Thin Solid Films* 516 (2008) 3282–3286.
- [20] J. Fondard, A. Billard, G. Bertrand, P. Briois, Synthesis and characterization of  $\text{La}_2\text{NiO}_4 + \delta$  coatings deposited by reactive magnetron sputtering using plasma emission monitoring, *Solid State Ionics* 265 (2014) 73–79.
- [21] A. Ringuedé, J. Foulletier, Oxygen reaction on strontium-doped lanthanum cobaltite dense electrodes at intermediate temperatures, *Solid State Ionics* 139 (2001) 167–177.
- [22] B.A. Boukamp, N. Hildebrand, P. Nammensma, D.H.A. Blank, the impedance of thin dense oxide cathodes, *Solid State Ionics* 192 (2011) 404–408.
- [23] A. Billard, C. Frantz, Attempted modelling of thickness and chemical heterogeneity in coatings prepared by d.c. reactive magnetron sputtering, *Surf. Coat. Technol.* 59 (1993) 41–47.
- [24] S. Schiller, G. Beister, W. Sieber, Reactive high rate D.C. sputtering: Deposition rate, stoichiometry and features of  $\text{TiO}_x$  and  $\text{TiN}_x$  films with respect to the target mode, *Thin Solid Films* 111 (1984) 259–268.
- [25] J. Fondard, P. Bertrand, A. Billard, S. Skrab, T. Franco, G. Bertrand, P. Briois, Synthesis of half fuel cell Ni-YSZ/YSZ on porous metallic support by dry surface deposition processes, *Electrochem. Soc. Trans.* 57 (2013) 673–682.
- [26] F. Perry, A. Billard, C. Frantz, An optical emission spectroscopy study of a reactive magnetron sputtering Ar- $\text{O}_2$  discharge modulated at low frequency, *Surf. Coat. Technol.* 94–95 (1997) 681–685.
- [27] F. Sanchette, T. Czerwicz, A. Billard, C. Frantz, Sputtering of Al-Cr and Al-Ti composite targets in pure Ar and in reactive Ar- $\text{N}_2$  plasmas, *Surf. Coat. Technol.* 96 (2–3) (1997) 184–190.
- [28] P.-L. Coddet, M.C. Pera, A. Billard, Reactive co-sputter deposition of YSZ coatings using plasma emission monitoring, *Surf. Coat. Technol.* 205 (2011) 3987–3991.
- [29] M. Zinkevich, F. Aldinger, Thermodynamic analysis of the ternary La-Ni-O, *J. Alloys Compd.* 375 (1–2) (2004) 147–161.
- [30] A. Anders, A structure zone diagram including plasma-based deposition and ion etching, *Thin Solid Films* 518 (2010) 4087–4090.
- [31] N. Hildenbrand, P. Nammensma, D.H.A. Blank, H.J.M. Bouwmeester, B.A. Boukamp, Influence of configuration and microstructure on performance of  $\text{La}_2\text{NiO}_{4+\delta}$  intermediate-temperature solid oxide fuel cells cathodes, *J. Power Sources* 238 (2013) 442–453.
- [32] H. Wang, W. Ji, L. Zhang, Y. Gong, B. Xie, Y. Jiang, Y. Song, Preparation of YSZ films by magnetron sputtering for anode-supported SOFC, *Solid State Ionics* 192 (2011) 413–418.
- [33] P. Coddet, M.C. Pera, A. Billard, Planar Solid Oxide Fuel Cell: Electrolyte Deposited by Reactive Magnetron Sputtering and Cell Test, *Fuel Cells* 11 (2) (2011) 158–164.
- [34] E.J.L. Schouler, M. Kleitz, Electrocatalysis and inductive effects at the gas, Pt/stabilized zirconia interface, *J. Electrochem. Soc.* 134 (1987) 1045–1050.
- [35] L. Mogni, N. Grunbaum, F. Prado, A. Caneiro, Oxygen reduction reaction on ruddlesden–popper phases studied by impedance spectroscopy, *J. Electrochem. Soc.* 158 (2011) B202–B207.